

Journal of Biomedical Optics

SPIEDigitalLibrary.org/jbo

Modulation of photoacoustic signal generation from metallic surfaces

Trevor Mitcham
Kimberly Homan
Wolfgang Frey
Yun-Sheng Chen
Stanislav Emelianov
John Hazle
Richard Bouchard

Modulation of photoacoustic signal generation from metallic surfaces

Trevor Mitcham,^a Kimberly Homan,^b Wolfgang Frey,^b Yun-Sheng Chen,^b Stanislav Emelianov,^{a,b} John Hazle,^a and Richard Bouchard^a

^aUniversity of Texas MD Anderson Cancer Center, Department of Imaging Physics, 1881 East Road Unit 1902, Houston, Texas 77054

^bUniversity of Texas at Austin, Department of Biomedical Engineering, 1 University Station C0800, Austin, Texas 78712

Abstract. The ability to image metallic implants is important for medical applications ranging from diagnosis to therapy. Photoacoustic (PA) imaging has been recently pursued as a means to localize metallic implants in soft tissue. The work presented herein investigates different mechanisms to modulate the PA signal generated by macroscopic metallic surfaces. Wires of five different metals are tested to simulate medical implants/tools, while surface roughness is altered or physical vapor deposition (PVD) coatings are added to change the wires' overall optical absorption. PA imaging data of the wires are acquired at 970 nm. Results indicate that PA signal generation predominately occurs in a wire's metallic surface and not its aqueous surroundings. PA signal generation is similar for all metals tested, while addition of PVD coatings offers significant modulations (i.e., 4-dB enhancement and 26-dB reduction achieved) in PA signal generation. Results also suggest that PA signal increases with increasing surface roughness. Different coating and roughness schemes are then successfully utilized to generate spatial PA signal patterns. This work demonstrates the potential of surface modifications to enhance or reduce PA signal generation to permit improved PA imaging of implants/tools (i.e., providing location/orientation information) or to allow PA imaging of surrounding tissue. © 2013 Society of Photo-Optical Instrumentation Engineers (SPIE) [DOI: 10.1117/1.JBO.18.5.056008]

Keywords: photoacoustics; medical imaging; metallic surface; implant visualization; implant patterning; image-guided.

Paper 12815R received Dec. 20, 2012; revised manuscript received Mar. 20, 2013; accepted for publication Apr. 4, 2013; published online May 7, 2013.

1 Introduction

Metallic implants and tools are utilized for a myriad of medical applications, including intraoperative tools [e.g., biopsy needles, surgical scalpels, or radiofrequency ablation (RFA) catheters], short-term implants (e.g., biopsy clips), and long-term implants (e.g., brachytherapy seeds and coronary stents). Clinical needles are used for minimally invasive tissue biopsies, as well as to provide local drug delivery,¹ while RFA catheters are used to treat cardiac arrhythmias, such as atrial fibrillation.² Short-term biopsy clips are placed at the site of a biopsy to allow for precise identification of a lesion, which helps to facilitate its complete surgical resection.³ Long-term implants are typically placed inside of the body to serve a therapeutic purpose, such as a stent providing relief for coronary heart disease,⁴ or a prostatic brachytherapy seed delivering localized radiation.⁵

Image guidance can assist in proper placement of metallic implants and improve the therapeutic efficacy of these procedures. Current imaging techniques used to visualize metallic implants in the body include x-ray-based imaging, such as fluoroscopy or x-ray computed tomography (CT),⁶ and ultrasonic (US) imaging.⁷ X-ray fluoroscopy is the most common method used to assess coronary stent position⁸ and to verify the location of prostatic brachytherapy seeds immediately following the implantation procedure,⁹ while x-ray CT is standardly used for quality assurance purposes to calculate brachytherapy seed radiation dosimetry.¹⁰ US imaging is commonly used for clinical needle guidance¹ and intraoperative guidance during brachytherapy seed implantation procedures.⁹ However, US and

x-ray-based modalities each have well noted limitations when imaging metal in the body. US images of metallic objects often provide poor contrast between tissue and the implant.¹¹ And although x-ray based techniques provide superior contrast between the implant and soft tissue, they can result in a significant dose of ionizing radiation to both the patient and the operator,^{12,13} and often fail to provide sufficient soft tissue contrast to determine anatomical context. In an effort to overcome the limitations with these current imaging techniques, photoacoustic (PA) imaging has recently been investigated to image metallic implants and surgical tools in soft tissue.^{5,14,15}

PA imaging relies on the photoacoustic effect, which occurs when a photoabsorber is irradiated with a pulsed laser beam, causing a thermal expansion response that creates a local acoustic source.¹⁶ These local pressure waves can then be detected and imaged with a conventional US detector. The pressure detected by the US probe is linearly related to the optical absorption coefficient of the absorber, as well as the local laser fluence; thus, PA signal amplitude provides an indication of local optical absorption in tissue. Initial PA pressure can be estimated by¹⁷

$$p_o = \left(\frac{\beta c^2}{C_p} \right) \mu_a F, \quad (1)$$

where $\beta[\text{K}^{-1}]$ is the thermal coefficient of volume expansion, $c[\text{m/s}]$ is the speed of sound in tissue, $C_p[\text{J}/(\text{kg K})]$ is the heat capacity at constant pressure, $\mu_a[\text{cm}^{-1}]$ is the optical absorption coefficient, and $F[\text{J}/\text{cm}^2]$ is the local laser fluence; the terms in the parentheses are known collectively as the Grüneisen parameter, or Γ . As optical absorption coefficients

Address all correspondence to: Richard Bouchard, University of Texas MD Anderson Cancer Center, Department of Imaging Physics, 1881 East Road Unit 1902, Houston, Texas 77054. Tel: 713-745-0626; Fax: 713-563-2986; E-mail: rbouchard@mdanderson.org

of metals in the near-infrared (NIR) range tend to be orders of magnitude higher than endogenous absorbers (e.g., hemoglobin), the PA signal generated by metal is typically much higher than the signal emanating from the surrounding tissue.⁹ Additionally, PA imaging can be supplemented with US imaging (i.e., PAUS imaging) to provide anatomical information of surrounding soft tissue.

Although PA imaging has been shown to offer superior contrast of metallic implants at shallow implantation depths, this contrast drops precipitously with increasing imaging depth due to the decreasing local fluence that results from tissue scattering.⁵ Local PA signal generation thus must be increased to facilitate increased PA imaging interrogation depths. Conversely, PA signal reduction would be useful for a clinician wishing to suppress the signal from an implant or tool to mitigate the interfering effects of their PA signal while obtaining PA imaging data of surrounding tissue during image-guided interventions (e.g., suppress signal from the catheter tip during PA-guided RFA therapy). Additionally, PA signal modulation (i.e., enhancement and reduction of PA signal) would allow for the placement of position markers along the length of needles or the reduction of signal generated by the shaft of a needle while leaving the tip highly visible to maintain location information. Therefore, the research presented herein focuses on mechanisms for enhancing, reducing, and patterning the PA signal generated by metallic implants and tools used in medicine.

In an effort to modulate the PA signal generated by metallic implants and tools, it was first necessary to determine whether the PA signal was generated from the metallic surface itself or the implant's surrounding water-based environment (i.e., soft tissue, blood, etc.). In the case of plasmonic nanoparticles, the PA signal is generated by the aqueous environment surrounding the particle.¹⁸ This was demonstrated by immersing nanoparticles in two different solvents—water and toluene—and showing that the magnitude of the resulting PA signal increased with increasing temperature (from 10 to 50°C) for water but generally decreased across the same range for toluene. This behavior was attributed to the fact that water's Grüneisen parameter, which is directly proportional to PA signal magnitude [Eq. (1)], increases with increasing temperature, while toluene's Grüneisen parameter tended to decrease with increasing temperature. Although the nanoparticles absorb the laser energy, the resulting heat is conducted to the environment, where thermal expansion and PA generation occur. An investigation into environmental effects on PA signal generation from macroscopic absorbers (i.e., implants/tools) will provide insight into which optical and/or thermomechanical material parameters must be manipulated in Eq. (1) to efficiently modulate signal generation.

If the PA signal is predominately generated in the surrounding aqueous environment, the rate of heat transfer from the metal surface to the environment becomes important. With gold nanorods, the PA signal generated in the environment surrounding the particles was shown to increase by adding a silica coating, which decreased the interfacial thermal resistance between the particles and their solvent.¹⁹ If the PA signal is predominately generated in the metallic surface of the implant/tool, however, then changing the surface's thermal coefficient of volume expansion [i.e., β from Eq. (1)] should affect signal generation. Regardless of the precise signal generation mechanism, the heat source in either case (i.e., PA signal generated in the environment or the surface) results from optical absorption by the metallic surface. Thus, based on Eq. (1), increasing the optical

absorption coefficient or local fluence or decreasing the heat capacity of the metallic surface should increase PA signal generation regardless of its origin. To alter the optical absorption (and β & C_p , in some cases), various biocompatible metals and physical vapor deposition (PVD) coatings with differing absorption coefficients were tested. Surface roughness or refractive index (i.e., by changing the material type) were also altered in an effort to modulate the total amount of energy that was transmitted (i.e., increasing F) into the surface and subsequently absorbed. Overall, the experiments presented herein were designed to demonstrate how PA signal from metallic objects is generated and how physical properties of the surface can be altered in order to modulate PA signal as needed for various clinical applications.

2 Materials and Methods

2.1 General Setup and Processing

To characterize the PA signal generated by different metallic surfaces and preparations, four imaging studies were conducted using 0.8-mm diameter wire as a target. Such a wire was chosen due to its similar width to that of a brachytherapy seed and its availability in a range of material types. The wire materials tested include: grade 2 titanium (Ti), type 304 stainless steel (304SS), type 316L stainless steel (316SS), nickel chromium (Chromel C) (all acquired from McMaster-Carr Supply Company, Elmhurst, IL), and grade 1 nickel titanium (Nitinol; Small Parts, Inc. c/o Amazon.com, LLC, Seattle, WA). As titanium is a material commonly used in most types of implants, all values were normalized relative to grade 2 titanium unless stated otherwise.^{5,20} All raw materials were chosen for their demonstrated biocompatibility as materials for medical implants or tools. Titanium is widely used to create orthopedic implants, dental implants, and prostatic brachytherapy seeds.^{5,20} Stainless steel is another commonly used material: type 304 is used for orthodontic implants, while type 316L is commonly utilized to produce orthopedic implants and coronary stents.^{21–23} Additionally, Nitinol is widely used in coronary stents and orthopedic implants.²⁴ Although there are current questions regarding the true biocompatibility of Chromel C, the material has been used historically in dental and orthodontic applications.²⁵

PA imaging studies were performed using the Vevo® LAZR-2100 PAUS imaging system (VisualSonics Inc., Toronto, Canada). A 24-mm-wide, 21-MHz, linear acoustic array transducer was used for signal detection and was coupled to the LAZR-2100 system for sample irradiation; the acoustic array is flanked by two optical fiber arrays that are positioned such that their transmitted line beams intersect 10 mm from the center of the array face, resulting in a spot size of approximately 72 mm² (i.e., 24 × 3 mm). All tests were performed at a laser wavelength of 970 nm with pulse energies of approximately 8 mJ. This wavelength, which is the highest laser wavelength supported by the LAZR-2100 system, was chosen as a higher wavelength would mitigate pulse attenuation due to scattering in tissue.

The imaging phantom (see Fig. 1) was constructed by suspending 21 wires across a plastic imaging tub. The tub included supports to ensure all wires rested at similar heights during imaging (right image of Fig. 1). Testing was performed at a depth of 10 mm in a solution of deionized (DI) water and 0.5% milk fat by volume, which was added to provide optical scattering in an effort to reduce the irradiation focal gain (i.e., to make the



Fig. 1 Photographs [(a) top view; (b) side view] of wire phantom loaded with 14 wires. Transducer shown in red with translation direction denoted.

imaging measurement less sensitive to height variation of the wires); the extinction coefficient of the scattering solution was 41 cm^{-1} (Ref. 26). All wires without a PVD coating were sanded uniformly with a new piece of 600-grit silicon carbide sandpaper (W.W. Grainger Inc., Lake Forrest, IL) for 45 s to provide a consistent surface roughness; sanded wires were then rinsed in a water bath to remove residual metallic shavings. No surface modifications resulted in a significant volumetric change in the wire. The linear array was translated 45 mm in the elevation dimension (see red arrows in Fig. 1) to obtain a three-dimensional (3-D) PA imaging data set; it was possible to image seven wires in each volume acquisition.

Quantitative analysis of the PA images was achieved by dividing an acquired imaging volume into isovolumetric regions centered around each wire within that imaging sub-volume. These regions were then divided equally length-wise to create 10 analysis kernels ($2.4 \text{ mm length} \times 2.5 \text{ mm width} \times 2.5 \text{ mm depth}$) for each wire. Background signal, in a region with the same depth range and lateral location but without a wire inclusion, was subtracted from the total signal for each kernel to obtain just the signal from the wire target and to remove the weak PA signal originating from the scattering milk-solution background. To mitigate PA signal differences due to depth variations, wires that were more than $500 \mu\text{m}$ from the mean imaging depth were excluded from analysis. Signal changes for each seven-wire acquisition were then calculated based on a Ti control that was contained in every seven-wire imaging subset; these normalization wires were necessary to account for local fluence variations (i.e., due to pulse-to-pulse variation, imaging depth differences, or scattering variations in different milk-solution preparations) between trials. Statistics were then calculated for the 10 kernels per wire for all wires of identical material or preparation (e.g., $n = 30$ for three wires or $n = 60$ for six wires). Statistical significance was calculated using a two-sample Student's t-test (two-tailed) with a significance level of 0.05. Tested data were compared with the control wire (sanded Ti) unless stated otherwise.

2.2 Environment Dependence

The first study investigated the difference in PA signal generated in different solvents as temperature increased. To achieve this, one Ti wire was placed in a vinyl tube containing toluene

(Sigma-Aldrich Corp., St. Louis, MO) and one Ti wire was placed in a tube containing water. The tubes were then sealed with epoxy and suspended in a temperature-controlled water bath of pure DI water. The temperature of the water bath was increased from 10 to 50°C , and PA data were acquired at increments of approximately 3°C . A 3-D PA scan was achieved along the length of each wire to provide five independent acquisition kernels for statistical analysis.

2.3 Raw Material Characterization

The second study compared the PA signal generated by different raw materials. Three separate tests were conducted, each with three Ti control wires and one wire of each tested metal, Nitinol, Chromel C, 304SS, and 316SS, for seven total wires per acquisition volume (i.e., 21 wires total). As described previously, all wires were sanded to establish a standard surface roughness between material types. Additionally, one of the three Ti control wires was used to normalize the PA signal of the other six wires in a seven-wire set.

2.4 Surface Roughness

2.4.1 Full-surface modification

The third study analyzed the effects of surface roughness on PA signal generation. This study compared the change in signal between wires of the same material with varied surface roughness. Four materials were tested: 316SS, Ti, Chromel C, and 304SS. Surface roughness was set with electropolishing, factory polishing, or 600-grit sanding. Chromel C and 304SS were available in a polished finish from the supplier, while the 316SS and Ti samples were electropolished (ABLE Electropolishing Co. Inc., Chicago, IL) to achieve a smooth finish. Electropolishing uses a rectified current and an electrolyte bath to remove the surface layer from metal, leaving behind a uniformly smooth surface of the pure metal.²⁷ Signal enhancement was then reported relative to the mean PA signal of the sanded preparation for each material type.

2.4.2 Patterning

After testing full-surface modification, another study was performed to create a distinct PA pattern on a surface. Within a

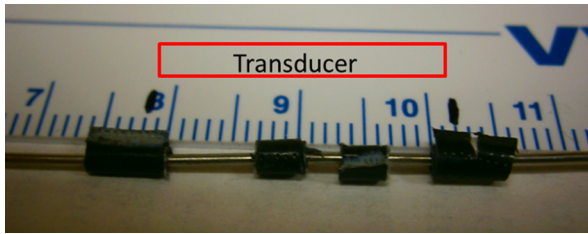


Fig. 2 Sample preparation for sanded pattern. Taped areas retained factory polish, while exposed areas were sanded with 600-grit sandpaper.

24-mm length of Chromel C wire, both edges as well as two sections in the middle were masked with duct tape (Fig. 2). The three inner exposed regions of the wire were then sanded with 600-grit sandpaper, producing distinct areas of roughness and smoothness along its length. PA imaging data were then acquired at 970 nm and reconstructed with 3-D rendering.

2.5 Surface Coatings

2.5.1 Full-wire coating

The final study compared the PA signal generated by wires with different PVD coatings applied (nominally 1 to 4 micrometers in thickness). Titanium, 316SS, and 304SS wires were PVD coated with: TiN, MoS₂, TiAlN, AlTiN, TiCN, ZrN, and AlTiSiN (Advanced Coating Technologies, Inc., Valencia, CA). These coatings were selected due to proven biocompatibility, as all have been either used in coating implants or have shown promise in clinical testing. Titanium nitride is widely used as a coating on orthopedic implants, while TiAlN and AlTiN are currently being explored for their biocompatibility potential.^{28–30} Zirconium nitride has demonstrated corrosion resistance and potential biocompatibility *in vitro*,³¹ while TiCN coatings have been shown to be neither cytotoxic nor genotoxic *in vitro*.²¹ Additionally, MoS₂ nanoparticles have been shown to be biocompatible.³² These coatings were applied to each of the aforementioned metal types (i.e., TiN was applied to one Ti, one 316SS, and one 304SS wire, and so forth). All wires were sent for coating in their default surface state from the factory, and the PVD coating surface state was maintained (i.e., PVD samples were not sanded) during testing. PA signal differences were calculated based on the signal from a sanded Ti reference wire included in each seven-wire imaging trial.

2.5.2 Patterning

In addition to testing full-wire coatings, the ability to create a pattern using PVD coatings was explored. The PVD coating pattern was formed by placing wires with different coatings adjacent to one another and by orienting the imaging transducer in the perpendicular axis (Fig. 3). A section of the block was removed below the patterned wire to mitigate the effect of reverberation during imaging. There were five total sections (three coated with MoS₂ and two coated with TiN). The sections alternated and contained a varying number of wire segments (3,3,4,4,5 wire sections from left to right in Fig. 3) to produce a unique pattern. The wire block was then imaged at 970 nm, and a PA B-mode image was generated of the resulting pattern.

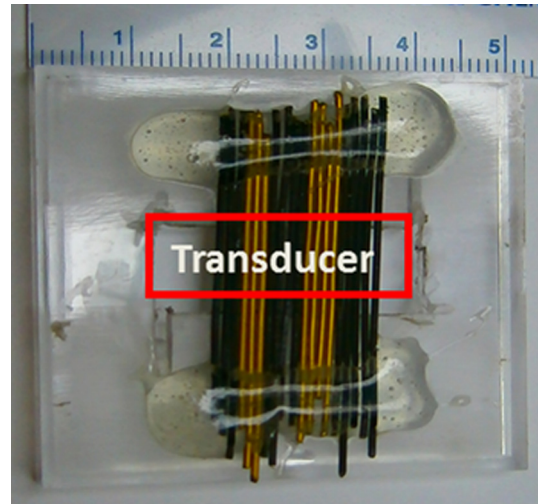


Fig. 3 Pattern created from physical vapor deposition (PVD)-coated wires. Black wires are coated with MoS₂; gold wires, TiN.

3 Results

3.1 Environment Dependence

The plot in Fig. 4 depicts the mean PA signal from Ti wires in water and toluene environments as temperature was increased from 10 to 50°C. The PA signal is normalized for each trace to the maximum PA signal, which occurred at 50°C for water and 41°C for toluene. Normalized PA signal increases of 34% and 24% were observed in the water and toluene environments, respectively.

3.2 Raw Material Characterization

The raw material characterization study demonstrated that metal type—of those tested—has little effect on the PA signal generated. All PA signals were normalized to the mean value of a Ti control wire. The only material to generate, on average, a PA signal of greater magnitude than that generated by Ti was Nitinol, with a mean enhancement of 0.21 dB. The 304SS and 316SS samples' mean PA signals yielded 0.78-dB and 0.93-dB reductions, respectively. None of these signal differences,

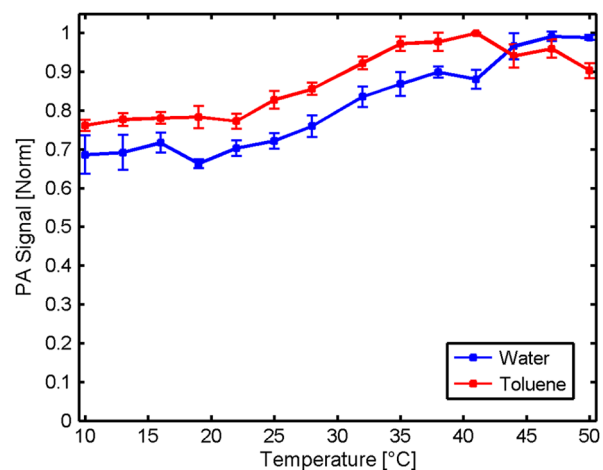


Fig. 4 PA signal ($n = 5$) from wire segments imaged while surrounded by water or toluene with increasing temperature.

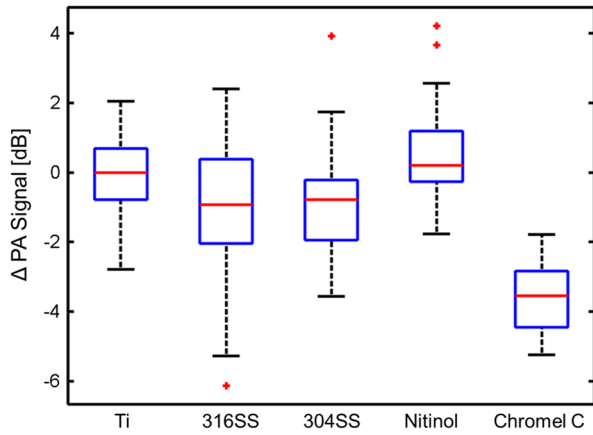


Fig. 5 PA signal response from sanded raw materials and normalized to Ti. Sample sizes: $n_{Ti} = 70$; $n_{Chromel-C} = 20$; $n_{Nitinol} = 20$; $n_{316SS} = 30$; $n_{304SS} = 30$.

however, were significant (Fig. 5). The only material that showed a significant signal change was the Chromel C wire, with a mean signal reduction 3.55 dB below the Ti control signal. Note that the mean, twenty-fifth percentile, and seventy-fifth percentile are depicted for each box plot, while a box's whiskers extend ± 2.7 standard deviations from the mean value. Outliers, which fall outside of this range, are denoted with single asterisks.

3.3 Surface Roughness

3.3.1 Full-surface modifications

Results from the surface modification study demonstrate that surface roughness can have a significant impact on the generated PA signal. As shown in Fig. 6, mean PA signal increases for all material types when sanded (when compared with their polished counterpart). When testing Chromel C wire, the factory polish produced a signal 6.38 dB below its sanded counterpart. Factory polished 304SS wires similarly generated a mean signal 1.94 dB lower than sanded 304SS wires. The signal further decreased when imaging electropolished wires. The electropolished 316SS mean signal decreased 11.87 dB from its sanded

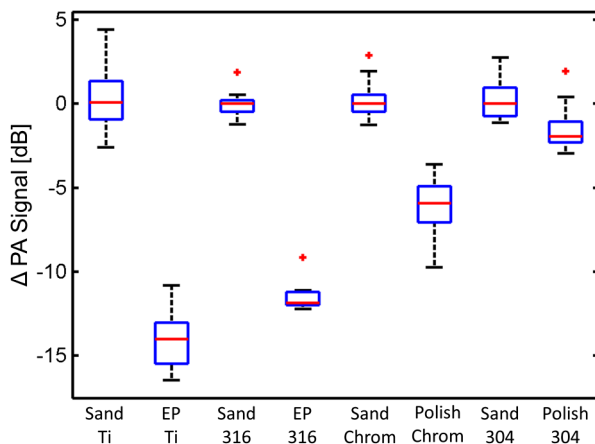


Fig. 6 Surface roughness testing at 970 nm. Sand: sanded material; EP: electropolished material; Polish: polished by manufacturer; Chrom: Chromel C. Sample sizes: $n_{Sand-Ti} = 30$; $n_{EP-Ti} = 20$; $n_{Sand-316SS} = 30$; $n_{EP-316SS} = 10$; $n_{Sand-Chromel-C} = 30$; $n_{Polish-Chromel-C} = 30$; $n_{Sand-304SS} = 30$; $n_{Polish-304SS} = 30$.

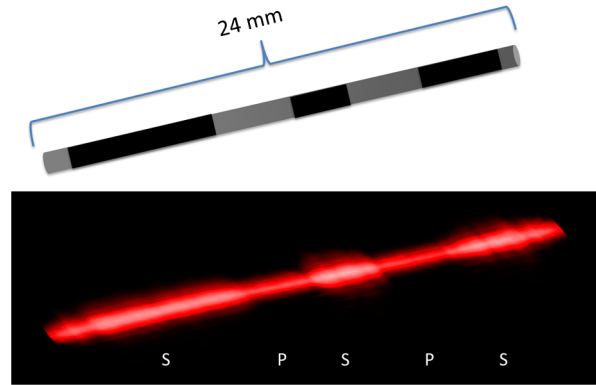


Fig. 7 Schematic (above) and 3-D-rendered PA image (below) of patterned (S: sanded section; P: polished section) wire from Fig. 2.

control, and the Ti mean signal decreased 14.02 dB after electropolishing.

3.3.2 Patterning

For the surface roughness pattern test, three sections of the wire were sanded, and two were left factory polished. The PA imaging 3-D rendering (Fig. 7) clearly shows areas of increased signal where the wire was sanded and areas of decreased signal where the factory polish was left unmodified. A 6-dB difference in PA signal was measured between adjacent pattern sections.

3.4 Surface Coatings

3.4.1 Full-surface coatings

Results from the surface coating study are presented in Fig. 8. Molybdenum disulfide produced the greatest signal enhancement, resulting in a mean signal enhancement of 3.93 dB (over its Ti control wire). Aluminum titanium nitride and AlTiSiN also provided signal enhancement, yielding mean enhancements of 0.56 and 0.99 dB, respectively. All the other coatings tested generated a mean decrease of the PA signal, with TiCN and TiAlN coatings resulting in mean reductions of 3.61 and 3.74 dB, respectively. The two most drastic signal reductions occurred with ZrN and TiN coatings, resulting in 17.69-dB and 25.75-dB reductions, respectively. It must be noted that the TiN

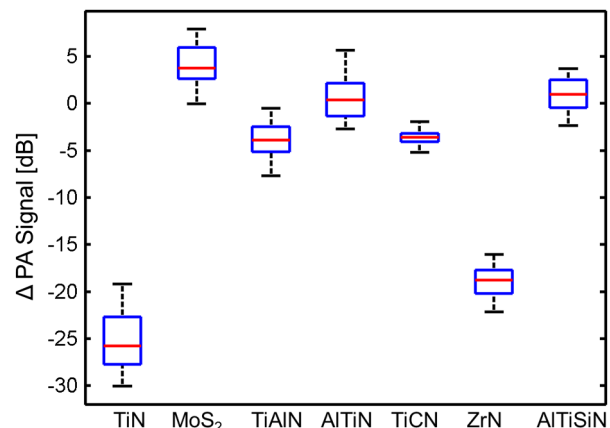


Fig. 8 PA signal generated from PVD coated wires ($n = 30$). Values normalized to uncoated Ti wire.

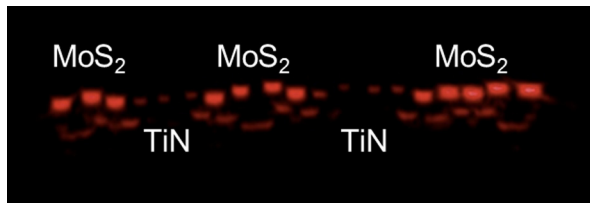


Fig. 9 PA signal of PVD-coated pattern phantom (Fig. 3). MoS₂ coating provides 30-dB signal enhancement over TiN coating to allow for implant patterning.

coating was not readily visible in many of the PA imaging trials. Aluminum titanium nitride was the only PVD coating that failed to produce a significantly different PA signal from that generated by the Ti control.

3.4.2 Surface coating patterning

Figure 9 presents a PA B-mode image from the surface coating pattern study depicted in Fig. 3. As is apparent in the PA image, segments coated with MoS₂ were significantly brighter than the TiN-coated wires, with a 30-dB signal differential observed. The MoS₂ coatings showed up very well in the generated PA image (Fig. 9), while the TiN-coated wires were not visually apparent. The fainter signal seen deep in the primary PA signal results from a comet-tail artifact that is generated due to reverberation within the wire targets.

4 Discussion

The results of this study demonstrate that it is possible to modulate (i.e., enhance or reduce) the PA signal generated from a metallic surface. The study of the environmental dependence suggests that a PA signal is predominately generated in the metal itself, not its surrounding environment. The type of metal used had little impact on the generated signal, while surface roughness and the application of a PVD coating were found, in some cases, to have a significant impact on the magnitude of the PA signal generation. In general, an increase in surface roughness of the material resulted in an increased PA signal. PVD coatings could be used to increase or decrease PA signal generation, with a 30-dB difference between MoS₂ (4-dB enhancement) and TiN (26-dB reduction) observed. In addition to successful full-surface modifications, the potential for PA patterning was demonstrated with the use of alternating PVD coatings or surface roughness. Future testing will investigate imaging modified implants in tissue-mimicking phantoms to acquire data closer to that which would be gathered *in vivo*.³³

Although all materials used have either been proven biocompatible via *in vitro* testing or are currently used as implantable materials in the body, not all materials are suitable for long-term implantation (e.g., low-dose rate brachytherapy). For instance, Chromel C has been used in dental implants, but some studies have shown that it may not be an effective material for long-term implantation due to its high nickel content.^{25,34} Additionally, sanding a material and increasing its surface roughness can lead to severely reduced biocompatibility and an increased failure rate;²⁴ this is especially true of devices such as stents and other small, load-bearing implants. However, not all implants are designed for long-term use. Some short-term implants, such as non-palpable breast lesion markers, are implanted and subsequently excised in a matter of days and would require less

stringent biocompatibility compliance due to their short duration inside the body.³⁵

In the environmental characterization experiment, the environment is shown to have little effect on the generated PA signal. Previous studies with plasmonic nanoparticles have shown that an approximate 300% increase and 40% decrease of the PA signal generated in water and toluene, respectively, can be observed through a 40° increase due to changes in the Grüneisen parameter of these solvents with increasing temperature.¹⁸ Therefore, the 34% increase observed in water—which was 10% higher than the increase observed in toluene—suggests that although there may have been a modest contribution from the water (i.e., due to heat conduction from the metallic surface), the majority of the PA signal was generated in the surface of the Ti, a material that should experience a modest increase in its Grüneisen parameter over the tested temperature range due to an increase in its thermal coefficient of volume expansion.^{36,37} Unpublished preliminary investigations into the use of silica coatings on macroscopic metallic surfaces failed to produce a PA signal enhancement. Given the high thermal conductivity of metals, the semi-infinite nature of the metallic body, which was hundreds of micrometers thick (compared with the optical absorption thickness, which was hundreds of nanometers in thickness), should function as a heat sink, discouraging immediate thermal conductivity into the surrounding environment.

Enhancements in PA signal resulting from sanding are possibly due to increases in surface area, multiple scattering resulting from diffuse reflection, and/or changes in oxide-layer-mediated transmittance. First, as surface area increases, the wire may be able to absorb more transmitted laser energy, thereby generating an increased signal. The absorption coefficient of the material itself is not changed, but rather there is a greater surface area available to absorb the energy. The sanded finish provides a greater surface area, as the sanding process creates microscopic ridges and texture across the surface. Polishing buffs out all of these micro-ridges to diminish the surface area, which would cause a weaker signal. Second, diffuse scattering, which is promoted by the rougher surface, could also allow for multiple scattering events, which would increase overall absorption as well. Third, sanding and electropolishing could affect the naturally occurring oxide layers (e.g., Cr₂O₃ and TiO₂) of the wires in different ways.^{38,39} Electropolishing removes a wire's native oxide layer, while sanding likely leaves regions of this layer intact. In the case of titanium, its naturally occurring oxide layer, TiO₂, has a refractive index (at 970 nm) that lies between the refractive indices of water and bare Ti; thus, the oxide layer could serve as a matching layer (i.e., increase transmittance).⁴⁰ Thus, electropolishing, which would remove this oxide layer, could also remove a matching layer, which would result in decreased transmittance and a decreased PA signal.

Additionally, in the case of stainless steel, the Cr₂O₃ passivation layer also affords the metal's surface a relatively high optical absorption (compared to its Fe₂O₃ counterpart, for example) at 970 nm.³⁸ Removal of a surface's passivation layer could result in a decrease in the optical absorption of the surface, partially offsetting the PA-signal-enhancing effects of the roughness created. Such a phenomenon would help explain why the polished 304SS samples presented a less drastic reduction in PA signal than the other materials tested (Fig. 6). It must also be noted that both factory polished samples yielded less drastic reductions than the electropolished samples. This discrepancy could be a result of varying degrees of sample smoothness

achieved with different polishing methods or the presence of an oxide-layer-mediated matching layer on the factory samples.

PA signal variations observed between PVD coatings are likely due to variations in transmissivity and/or absorption. The graphite-like appearance of MoS₂ suggests that the coating has high optical absorption, which would account for the PA signal increase it generated. Titanium nitride and ZrN coatings both have relatively high reflectances at 970 nm.⁴¹ An increase in reflectivity would result in a decrease in local fluence into the surface, which would yield a lower PA signal [see Eq. (1)].

Enhancement of the PA signal provides perhaps the most straightforward benefit for imaging metallic implants: increased imaging depth and/or improved contrast between the implant and surrounding soft tissue. Less obvious, but of equal importance, are the benefits of reducing the PA signal of an implant or tool. A TiN-coated scalpel would allow for imaging of surrounding endogenous absorbers (e.g., hemoglobin) in order to assess oxygen saturation in real-time during a surgical procedure, while a PVD-coated RFA catheter could allow for PA-imaging guidance of cardiac ablation with minimal interference from PA signal generated by the metallic tip. Additionally, both enhancement and reduction of PA signal can be combined on an implant or tool to produce a distinct pattern. Such a patterning technique could be useful for a clinical needle: coat the tip with a PA-enhancing material (e.g., MoS₂), but coat the rest of the shaft with a PA-reducing material (e.g., TiN) to mitigate interference with tissue visualization. A pattern could also enable clinicians to verify implant alignment *in vivo* or to promote uniform PA signal from an implant that varies in depth (e.g., increase surface roughness with implant depth).

5 Conclusion

This study demonstrates the potential to tailor the surface of a surgical implant or tool for improved PA-imaging guidance/visualization during clinical procedures. Additionally, results indicate that the PA signal is mostly generated within a metallic surface—and not its aqueous surroundings—for macroscopic objects. Mean PA signal generation was similar for all metals tested (generally within 1 dB), while addition of PVD coatings offered significant modulations in PA signal generation, with an enhancement of 4 dB and reduction of 26 dB achieved with MoS₂ and TiN, respectively. Results also indicate that the PA signal increases with increasing surface roughness. Different coating and surface roughness schemes were successfully utilized to generate PA signal patterns on metallic phantoms. This work establishes the ability of surface modifications to enhance the efficacy of imaging metallic implants or their tissue surroundings photoacoustically through PA signal enhancement (i.e., to permit deeper imaging), PA signal reduction (i.e., to provide a “stealth” implant), or a combination of the two phenomena (i.e., to create a spatial pattern).

Acknowledgments

This work was supported by a Prostate Cancer SPORE Developmental Research Program award (P50 CA140388) from the National Cancer Institute and by the Odyssey Program and the Laura and John Arnold Foundation at the University of Texas MD Anderson Cancer Center. Imaging studies were conducted at the Small Animal Imaging Facility at the University of Texas MD Anderson Cancer Center with the help of Charles Kingsley and Jorge De La Cerda.

References

1. J. W. Charboneau, C. C. Reading, and T. J. Welch, “CT and sonographically guided needle biopsy: current techniques and new innovations,” *Am. J. Roentgenol.* **154**(1), 1–10 (1990).
2. R. Bouchard et al., “Photoacoustic characterization of radiofrequency ablation lesions,” *Proc. SPIE* **8223**, 82233K (2012).
3. L. Liberman et al., “Clip placement after stereotactic vacuum-assisted breast biopsy,” *Radiology* **205**(2), 417–422 (1997).
4. J. L.-S. Su, B. Wang, and S. Y. Emelianov, “Photoacoustic imaging of coronary artery stents,” *Opt. Express* **17**(22), 19894–19901 (2009).
5. J. L. Su et al., “Photoacoustic imaging of prostate brachytherapy seeds,” *Biomed. Opt. Express* **2**(8), 2243–2254 (2011).
6. S. J. Braak et al., “Real-time 3D fluoroscopy guidance during needle interventions: technique, accuracy, and feasibility,” *Am. J. Roentgenol.* **194**(5), W445–W451 (2010).
7. J. Su et al., “Photoacoustic imaging of clinical metal needles in tissue,” *J. Biomed. Opt.* **15**(2), 021309 (2010).
8. D. R. Elgort et al., “Image guided and monitored renal artery stenting using only MRI,” *J. Mag. Res. Imag.* **23**(5), 619–627 (2006).
9. J. L. Su et al., “Photoacoustic imaging of prostate brachytherapy seeds,” *Biomed. Opt. Express* **2**(8), 2243–2254 (2011).
10. Y. Su et al., “Prostate brachytherapy seed localization by analysis of multiple projections: identifying and addressing the seed overlap problem,” *Med. Phys.* **31**(5), 1277–1287 (2004).
11. W. Xu, S. E. Salcudean, and P. D. Lawrence, “Detection of brachytherapy seeds using 3-D transrectal ultrasound,” *IEEE Trans. Biomed. Eng.* **57**(10), 2467–2477 (2010).
12. Y. R. Rampersaud et al., “Radiation exposure to the spine surgeon during fluoroscopically assisted pedicle screw insertion,” *Spine* **25**(20), 2637–2645 (2000).
13. M. Mahesh, “Fluoroscopy: patient radiation exposure issues,” *Radiograph. J. Continuing Med. Edu. Radiol.* **21**(4), 1033–1045 (2001).
14. T. Harrison and R. J. Zemp, “Coregistered photoacoustic-ultrasound imaging applied to brachytherapy,” *J. Biomed. Opt.* **16**(8), 080502 (2011).
15. N. Kuo et al., “Real-time photoacoustic imaging of prostate brachytherapy seeds using a clinical ultrasound system,” *J. Biomed. Opt.* **17**(6), 066005 (2012).
16. M. Xu and L. V. Wang, “Photoacoustic imaging in biomedicine,” *Rev. Sci. Instrum.* **77**(4), 041101 (2006).
17. A. Oraevsky and A. Karabutov, “Optoacoustic tomography,” *Biomed. Phot. Handbook* **34**, 1–34 (2003).
18. Y. S. Chen et al., “Environment dependent generation of photoacoustic waves from plasmonic nanoparticles,” *Small* **8**(1), 47–52 (2012).
19. Y. S. Chen et al., “Silica-coated gold nanorods as photoacoustic signal nano-amplifiers,” *Nano Lett.* **11**(2), 348–354 (2011).
20. D. M. Brunette, *Titanium in Medicine: Material Science, Surface Science, Engineering, Biological Responses & Medical Applications*, Springer, Berlin (2001).
21. R. A. Antunes et al., “Study of the corrosion resistance and *in vitro* biocompatibility of PVD TiCN-coated AISI 316L austenitic stainless steel for orthopedic applications,” *Surf. Coat. Tech.* **205**(7), 2074–2081 (2010).
22. T. Duerig, A. Pelton, and D. Stöckel, “An overview of nitinol medical applications,” *Mater. Sci. Eng. A* **273**, 149–160 (1999).
23. F. L. Nie et al., “Comparative study on corrosion resistance and *in vitro* biocompatibility of bulk nanocrystalline and microcrystalline biomedical 304 stainless steel,” *Dent. Mater.* **27**(7), 677–683 (2011).
24. S. A. Shabalovskaya, “Surface, corrosion and biocompatibility aspects of Nitinol as an implant material,” *Biomed. Mater. Eng.* **12**(1), 69–109 (2002).
25. J. D. Bumgardner and L. C. Lucas, “Corrosion and cell culture evaluations of nickel-chromium dental casting alloys,” *J. Appl. Biomater.* **5**(3), 203–213 (1994).
26. W. R. Calhoun et al., “Sensitive real-time measurement of the refractive index and attenuation coefficient of milk and milk-cream mixtures,” *J. Dairy Sci.* **93**(8), 3497–3504 (2010).
27. E. S. Lee, “Machining characteristics of the electropolishing of stainless steel (STS316L),” *Int. J. Adv. Manu. Tech.* **16**(8), 591–599 (2000).
28. A. L. Paschoal et al., “Metallic biomaterials TiN-coated: corrosion analysis and biocompatibility,” *Artif. Organs* **27**(5), 461–464 (2003).

29. M. Braic et al., "Synthesis and characterization of TiN, TiAlN and TiN/TiAlN biocompatible coatings," *Surf. Coating. Technol.* **200**(1-4), 1014-1017 (2005).
30. M. Pellman, "PVD coatings for medical device applications," *Products Finishing* **64**(10), 116-123 (2000).
31. Y. Xin et al., "Corrosion behavior of ZrN/Zr coated biomedical AZ91 magnesium alloy," *Surf. Coating. Technol.* **203**(17), 2554-2557 (2009).
32. H. Wu et al., "Biocompatible inorganic fullerene-like molybdenum disulfide nanoparticles produced by pulsed laser ablation in water," *ACS Nano* **5**(2), 1276-1281 (2011).
33. J. R. Cook, R. R. Bouchard, and S. Y. Emelianov, "Tissue-mimicking phantoms for photoacoustic and ultrasonic imaging," *Biomed. Opt. Express* **2**(11), 3193-3206 (2011).
34. J. Bumgardner and L. Lucas, "Cellular response to metallic ions released from nickel-chromium dental alloys," *J. Dent. Res.* **74**(8), 1521-1527 (1995).
35. J. W. Jakub et al., "Current status of radioactive seed for localization of non palpable breast lesions," *Am. J. Surg.* **199**(4), 522-528 (2010).
36. F. Cervera, *ASM Ready Reference: Thermal Properties of Metals*, ASM International, Ohio (2002).
37. E. Collings, *Materials Properties Handbook: Titanium Alloys*, ASM International, Ohio (1994).
38. B. Karlsson et al., "Optical-properties of some metal-oxides in solar absorbers," *Phys. Scripta* **25**(6), 826-831 (1982).
39. Z. Y. Han et al., "Synthesis and photoelectric property of poly(3-pctylthiophene)/titanium dioxide hybrid," *J. Inorg. Organomet. P* **20**(1), 32-37 (2010).
40. J. R. DeVore, "Refractive indices of rutile and sphalerite," *J. Opt. Soc. Am.* **41**(6), 416-417 (1951).
41. B. Karlsson et al., "Optical properties of CVD-coated TiN, ZrN and HfN," *Sol. Energ. Mater.* **7**(4), 401-411 (1983).